LES BASED TRAILING-EDGE NOISE PREDICITON

W. SCHRÖDER, M. MEINKE, R. EWERT AND W.A. EL-ASKARY

Aerodynamisches Institut, RWTH Aachen
Wüllnerstr. 5-7, 52062 Aachen, Germany

Abstract. The paper presents a large-eddy simulation of the flow over a sharp trailing edge. To minimize the computational effort inflow conditions for fully turbulent compressible boundary layers are developed. The LES findings show good agreement with other numerical and experimental data. For the prediction of the trailing-edge noise, acoustic perturbation equations are derived, which are excited by sources determined from results of a compressible flow simulation. Results of acoustic fields are presented for a model problem.

1. Introduction

The interaction of the turbulent boundary layer and the wake in the vicinity of a trailing edge produces noise [6]. For the prediction of the trailing-edge aeroacoustics a two-step approach is proposed. The first step consists of a large-eddy simulation of the compressible flow problem only in the area where the noise is generated, i.e., just in the immediate vicinity of the trailing edge. Since the acoustical and fluid dynamical length scales differ considerably, the acoustic field is computed with a different grid resolution in a second step, using a system of acoustic perturbation equations that describe only the propagation of the acoustic modes. Its computational domain contains not only the trailing-edge region but the entire plate. Source terms, determined from the LES solution, are used to generate the sound in the trailing-edge region. Since only the aft region of the plate geometry is simulated in the LES, appropriate inflow conditions for a turbulent compressible boundary layer are derived. In the second part of the paper the acoustic perturbation equations are briefly introduced and their prediction qualities are discussed based on the flow over a circular cylinder [3]. In an upcoming step the trailing-edge noise will be simulated.

2. LES of the Trailing-Edge Flow

2.1. NUMERICAL METHOD AND CONFIGURATION

A large-eddy simulation is performed to simulate the turbulent compressible flow over a sharp trailing-edge of an adiabatic flat plate. The discretization of the convective fluxes in the governing equations is a second-order accurate AUSM formulation with a central pressure derivative. The viscous stresses are discretized using central differences of second-order accuracy. Furthermore, an explicit 5-step Runge-Kutta time stepping scheme of second-order accuracy is used for the temporal integration. The scheme is described in more detail in [9] where also results of various validation tests are discussed. The flow being simulated corresponds to experiments conducted by the Universities of Dresden and Stuttgart at a Reynolds number based on the freestream velocity and the length of the plate of Re_∞=5.33·10^5 and a Mach number of M=0.15 [10]. The thickness d of the plate is linearly reduced from d=1mm to zero under an angle of 15^o to avoid vortex shedding in the wake. Hot wire measurements are used to determine the mean velocity and turbulence intensities in the boundary layer and the wake. To reduce the computational effort while capturing the essential physics the numerical simulations are conducted in a domain that contains 25% of the total length of the plate. Since the boundary layer is tripped immediately after the leading edge, a fully turbulent boundary layer enters the domain of integration with a thickness of δ_0/d=2.1.

2.2. BOUNDARY CONDITIONS

The domain of integration comprises only the rear part of the flat plate and the wake region. Therefore, a slicing technique is used in which the instantaneous velocity distribution at each time level for the inflow boundary is generated from the simultaneous simulation of a turbulent boundary layer, see Fig. 6. The boundary layer simulation also requires an inlet boundary condition, which is obtained by extending the method of Lund et al. [8] for compressible flows. This technique will be discussed in the next section. At the surface of the plate the no-slip condition and an adiabatic wall is prescribed, at all outflow boundaries non-reflecting boundary conditions with pressure relaxation are applied [11]. Since the pressure relaxation introduces some numerical reflections, a sponge layer zone is added, in which the source terms S are computed as a function of the deviation of the instantaneous from the analytical solution q_a based on the logarithmic wall law $S = \sigma(q(t,\vec{x}) - q_a(\vec{x}))$, where q represents the vector of conservative variables. The parameter σ is computed as a function of the distance from the boundaries and increases from zero to σ_{max} within the sponge layer zone. The value for σ_{max} is chosen to be 0.5, which has been determined in test simulations under the condition to minimize numerical reflections.

2.3. RESCALING METHOD

The slicing technique involves the simulation of an adiabatic flat plate boundary layer. For that purpose the rescaling method of Lund et al. [8] is extended for compressible flows. In a first attempt a constant total enthalpy in the inflow section of the boundary layer was assumed, so that the mean and the fluctuation temperature could be determined by the corresponding velocity quantities. This procedure was called simple temperature rescaling [2]. The results, however, showed quite a discrepancy in the mean streamwise velocity (Fig. 1) and the skin-friction distribution (Fig. 2), which is why a more consistent compressible extension of the rescaling method was derived. The idea of the rescaling method is to decompose all flow field components into a mean and a fluctuating part, and then, to apply an appropriate scaling law to each quantity separately for inner and outer layers. For the velocity components the procedure proposed by Lund et al. [8] is adopted.

To take into account compressibility effects the temperature profile is rescaled as follows. For the mean static temperature T, we locally use Walz's equation $T/T_\infty = 1 + A(1 - U^2/U_\infty^2)$ with $A = 0.5(\gamma - 1)rM^2$, where r represents the recovery factor and M the freestream Mach number [14]. Furthermore, the temperature fluctuation T' can be calculated assuming a negligible total temperature fluctuation T_t' compared with the static temperature fluctuation. This assumption is valid, since we study subsonic flows at $M = 0.4$ and $M = 0.15$ in the present work. Following Bradshaw [1], we introduce the static temperature fluctuation

$$\frac{T'(y,z,t)}{T(y,z,t)} = -(\gamma - 1)\, M_l^2 \frac{u_1'(y,z,t)}{u_1(y,z,t)} \quad ,$$

where M_l is the local Mach number. Using the equation of Walz [14] and formulating the rescaling process similar to the velocity we obtain the following equations for the rescaled temperature and its fluctuations

$$T_{in}^{inner} = \beta_s^2 T_{re}(y_{in}^+) + C_1 T_\infty \quad \text{and} \quad T_{in}^{outer} = \beta_s^2 T_{re}(\eta_{in}) - C_2 \frac{U_{re}(\eta_{in})}{U_\infty} T_\infty + C_3 T_\infty$$

$$T'^{inner}_{in} = \beta_s^2 T'_{re}(y_{in}^+, z, t) \quad \text{and} \quad T'^{outer}_{in} = \beta_s^2 T'_{re}(\eta_{in}, z, t) - C_2 \frac{(u_1')_{re}(\eta_{in}, z, t)}{U_\infty} T_\infty$$

with $C_1 = (1 + A)(1 - \beta_s^2)$, $C_2 = 2A\beta_s(1 - \beta_s)$, and $C_3 = (1 - \beta_s)(1 + \beta_s + 2A\beta_s)$. If the rescaling factor $\beta_s = u_{\tau,in}/u_{\tau,re}$ is assumed to be 1 for the temperature distribution, we arrive at the formulation that was used by Urbin et al. [13] to compute supersonic boundary layers.

The composite distribution that is approximately valid over the entire boundary layer is obtained by forming a weighted average of the inner and outer profile for the velocity and the temperature as was proposed by Lund et al. [8].

The rescaling operation requires the skin friction velocity u_τ and the boundary layer thickness δ, both at the rescaling station and at the inlet. They can be directly determined from the mean velocity profile at the rescaling station, but must be specified at the inlet. It is sufficient to fix δ at the inlet, whereas u_τ for compressible flow at the inlet is evaluated via

$$u_{\tau,in} = u_{\tau,re}\sqrt{\left(\frac{\rho_{(wall)_{re}}}{\rho_{(wall)_{in}}}\right)}\left(\frac{\delta_{1re}}{\delta_{1in}}\right)^{\frac{1}{[2(n-1)]}}$$

where δ_1 is the displacement thickness, $\rho_{(wall)}$ is the local density at the wall, the ratio of which contains the temperature distribution along the surface, and the exponent n is set to n=5. The above relation can be derived from the standard power-law approximations, $c_f \sim Re_x^{1/n}$, $\delta_1/x \sim Re_x^{1/n}$, where c_f is the skin-friction coefficient. Unlike in Lund et al. [8] where the momentum thickness is used we incorporate the displacement thickness in the rescaling formulation. Since the momentum thickness is a non-linear function of the velocity profile, different results are obtained when either the spanwise averaged velocity profile is used to compute the momentum thickness or the momentum thickness is computed locally and then averaged in the spanwise direction.

2.4. RESULTS

To validate the compressible rescaling method we first simulate a boundary layer flow of an adiabatic flat plate for M=0.4 and Re_{δ_o}=14400 (Re_{θ_o}=1400), where δ_o is the boundary layer and θ_o the momentum thickness at the inlet, respectively. The dimensions of the computational domain are $30\delta_0 \times 3.5\delta_0 \times 0.64\delta_0$ in the streamwise, wall normal, and spanwise direction. Furthermore, we evidence the influence of the sponge layer and study the impact of grid resolution by using two different grids, one with approx. 700,000 cells and a finer mesh with approx. 1,350,000 cells.

The mean streamwise velocity profiles are plotted in inner-law scaling in Fig. 1 for both grid resolutions and different rescaling laws. The fine grid profiles based on the new temperature rescaling closely follow the analytic form that consists of the viscous sublayer $y^+ \leq 5$, $u/u_\tau = y^+$, the buffer layer $5.0 < y^+ \leq 30.0$, $u/u_\tau = 5.0 \ln y^+ - 3.05$, and the logarithmic layer $y^+ > 30.0$, $u/u_\tau = 2.5 \ln y^+ + 5.5$. In Fig. 2 the skin friction coefficient is compared with the formula of Falkner $c_f = 0.012/Re_\theta^{\frac{1}{6}}$ [4]. Here, also results of a coarse grid solution using no sponge layer are shown to demonstrate the influence of the formulation of the exit boundary condition. The added source term in the sponge layer damps reflected pressure waves, but also all turbulent fluctuations, so that c_f is progressively reduced in the sponge layer region. c_f is slightly underpredicted on the coarse grid, since the coherent structures

that redistribute the turbulence intensities from the streamwise direction to the wall normal and spanwise directions are not captured accurately with the larger spatial steps. Consequently, this leads to a smaller exchange of momentum, and thus, to a lower wall shear stress on the coarse grid. The turbulence intensities are compared in Fig. 5 with the data of Lund et al. [8] at $Re_\theta = 1850$ for the fine grid. The good agreement of the present results of a compressible boundary layer and the LES of Lund et al. [8] is clearly visible.

Fig. 3 shows the mean temperature distribution in inner-law scaling y^+. The profiles do not coincide perfectly near the inflow section, whereas further downstream the distributions do lie on top of each other up to the beginning of the outer layer at approx. y^+=180. The discrepancy immediately downstream of the inlet probably occurs due to the linear interpolation for corresponding locations at the inlet and rescaling locations and the different grid resolution, which, measured in wall units, is coarser at the inlet than further downstream. Fig. 4 illustrates the mean temperature-velocity relationship. The simulation data fits well with the Walz's quadratic profile for an adiabatic wall [14].

Using the compressible boundary layer solution, a realistic inlet boundary condition is obtained for the turbulent trailing-edge flow. The grid lines at the inflow boundary coincide with those of the boundary layer simulation, such that no interpolation of the instantaneous solution is required. The entire computational mesh to simulate trailing-edge flow is plotted in Fig. 7. It contains 2,250,000 grid points distributed in 19 blocks, 3 blocks of which are used for the flat plate simulation. To evidence the vortical structures in the vicinity of the trailing edge, the wake of the M=0.15 flow is visualized using the λ_2-criterion [7] in Fig. 8. The initially elongated vortex structures above the plate become shorter close to the trailing edge due to the deceleration of the flow.

In Figs. 9 and 10 mean velocity and turbulence intensity profiles in the trailing-edge and near-wake regions are compared with the experimental data from [10]. The agreement of the turbulence intensity between the present LES and the experimental data is fairly good except in the near-wall region where the experimental intensity profiles lack the near-wall peaks that do exist in turbulent boundary layers. This suggests a spatial underresolution or an insufficient high-frequency response of the measuring instrument near the wall.

The time history of the flow induced force on the plate in the vertical direction is plotted in Fig. 11. These fluctuations occur with a regular frequency related to a Strouhal number of about 0.2 based on the plate thickness. Thus, they are obviously associated with a Kelvin-Helmholtz type unsteady motion in the wake of the trailing edge, which can clearly be seen in the spanwise averaged temperature distribution in Fig. 12. Since

the unsteady vorticity in the wake has a vortex axis parallel to the trailing edge, it produces more efficient sound than the turbulent eddies from the boundary layer, which are more aligned with the streamwise direction.

3. Simulation of Aerodynamic Noise

We now turn to the numerical prediction of the acoustic field. The following discussion is a brief summary of the detailed analysis by Ewert et al. presented in [3]. The acoustic perturbation equations (APE) for the simulation of wave propagation are derived by a flow decomposition into acoustic and non-acoustic quantities, based on a filtering of the non-linear and viscous terms of the Navier-Stokes equations in Fourier/Laplace transformed space. The pressure is decomposed into a pseudo-sound pressure $\rho_\infty \phi_v$ and an acoustic perturbation p'. The perturbation density ρ' in general also contains non-acoustic fluctuations. Furthermore, the APE describe the propagation of irrotational velocities u' in an unsteady solenoidal background flow field U.

To compute the acoustic field of a circular cylinder at laminar freestream conditions the following simplifications are introduced. Neglecting the scattering of acoustic waves due to the unsteady mean-flow field, it seems to be acceptable to use a time averaged base flow field $\bar{U}_i$ instead of U_i. Furthermore, for small acoustic quantities the non-linear terms can be dropped. The equations used for the computations read, see [3] for details

$$\frac{\partial \rho'}{\partial t} + \frac{\partial}{\partial x_i}\left(\rho' \bar{U}_i + \rho_\infty u_i\right) = 0 \quad , \quad \frac{\partial u_i}{\partial t} + \frac{\partial}{\partial x_i}\left(\bar{U}_j u_j\right) + \frac{1}{\rho_\infty}\frac{\partial p'}{\partial x_i} = 0 \quad ,$$

$$\frac{\bar{D}p'}{Dt} - c_\infty^2 \frac{\bar{D}\rho'}{Dt} = -\rho_\infty \frac{\bar{D}\Phi v}{Dt} = -\rho_\infty \left(\frac{\partial \phi_v}{\partial t} + \bar{U}_i \frac{\partial \phi_v}{\partial x_i}\right) .$$

The term $\bar{D}\phi_v/Dt$ is computed by solving a Poisson equation with a right hand side determined from an appropriate LES or DNS solution of the compressible flow problem in the region where the noise is generated. The generation of vorticity is prevented completely. $\bar{U}_i$ is determined in the complete acoustic domain e.g. by an Euler or RANS computation. The acoustic field is computed by solving the perturbation equations for the unknowns ρ', u_i, p'.

3.1. NUMERICAL METHOD

For the spatial discretization of the acoustic perturbation equations the fourth-order dispersion relation preserving (DRP) scheme following Tam [12] is applied in generalized curvilinear coordinates. The DRP scheme is also applied to compute the metric terms so that a consistent discrete system is achieved. The temporal integration is performed using the fourth-order alternating two-step low dissipation and low dispersion Runge-Kutta scheme

(LDDRK 5-6). To suppress spurious high frequency waves artificial selective damping has been used. At far field boundaries a sponge layer formulation is used and at the solid walls a ghost point concept is imposed [3].

3.2. RESULTS

The flow around a circular cylinder at a freestream Mach number M=0.3 and a freestream Reynolds number based on the diameter Re_∞=200 is considered. The aeroacoustic sources are determined from a highly resolved compressible flow simulation. The solution of the acoustic perturbation equations with the source term determined by the unsteady flow, is performed on an O-grid with 257 × 161 grid points. The source terms are determined for 43 time levels within one vortex shedding cycle. During the acoustic simulation the time dependent source term for the intermediate time steps is computed using linear interpolation.

The acoustic pressure field $p - \rho_\infty \phi_v$ is shown in Fig. 13. According to the formulation of the acoustic perturbation equations no vorticity is generated by the acoustic simulation, so that no vortex street occurs. The directivity shown in Fig. 14 agrees well with that determined by Guo [5]. Since ϕ_v decays very fast to zero in a certain distance from the noise generating region the computation of the source term, e.g. from the large-eddy simulation, can be restricted to the small part of the total computational domain in which the noise generation occurs.

4. Conclusions

A consistent extension of the rescaling method for incompressible turbulent boundary layers to compressible fluids has been developed. Although only subsonic flows were considered at present, the results indicate that the proposed rescaling of the temperature profile seems to be superior to simpler formulations. An LES of the flow past a sharp trailing edge showed good agreement with experimental data. Furthermore, the acoustic field of the flow over a cylinder was computed using acoustic perturbation equations driven by a source term from the unsteady flow. The study proved the two-step approach to be capable to predict aeroacoustic sound based on a LES of a compressible flow field and will be used to predict trailing-edge noise in the next step.

References

1. P. Bradshaw. Compressible turbulent shear layers. *Ann. Rev. Fluid Mech*, 9:33–54, 1977.
2. R. Ewert, W. El-Askary, M. Meinke, and W. Schröder. Computation of turbulence related noise on the basis of large-eddy simulation. In H. Krner and J. W. Delfs, editors, *Second Aeroacoustics Workshop*. DLR Braunschweig, Oct. 2000.

3. R. Ewert, M. Meinke, and W. Schröder. Comparison of source term formulations for a hybrid CFD/CAA method. Paper 2001-2200, AIAA, 2001.
4. V. M. Falkner. The resistance of a smooth flat plate with turbulent boundary layer. *Aircraft Eng.*, 15:65–68, 1943.
5. Y. P. Guo. Application of the Ffowcs Williams/Hawkings equation to tw o dimensional problems. *J. Fluid Mech.*, 403:201–221, 2000.
6. M. S. Howe. Trailing edge noise at low mach numbers. *J. Sound and Vibration*, 225(2):211–238, 2000.
7. J. Jeong and F. Hussain. On the identification of a vortex. *J. Fluid Mech.*, 285:69–94, 1995.
8. T. S. Lund, X. Wu, and D. Squires. Generation of turbulent inflow data for spatially-developing boundary layer simulations. *J. of Computational Physics*, 140:233–258, 1998.
9. M. Meinke, W. Schröder, E. Krause, and T. Rister. A comparison of second- and sixth-order methods for large-eddy simulations. *Computers and Fluids*, pages –, submitted for publication, 2001.
10. J. Ostertag, S. Guidati, G. Guidati, S. Wagner, A. Wilde, and N. Kalitzin. Prediction and measurement of airframe noise on a generic body. Paper 2000-2063, AIAA, 2000.
11. T. J. Poinsot and S. K. Lele. Boundary conditions for direct simulations of compressible viscous flows. *J. Comput. Phys.*, 101:104–129, 1992.
12. C. Tam and J. Webb. Dispersion-relation-preserving finite difference schemes for computational acoustics. *J. Comput. Phys.*, 107:262–281, 1993.
13. G. Urbin and D. Knight. Compressible large eddy simulation using unstructured grid: supersonic boundary layer. In *Second AFOSR International Conference on DNS/LES, Rutgers University*, pages 1–16, June 7-9 1999.
14. A. Walz. *Boundary layers of flow and temperature.* MIT Press, 1969.

5. Figures

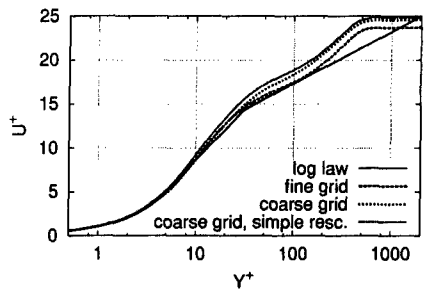

Figure 1. LES of a turbulent boundary layer for Re_{θ_o}=1400 and M=0.4 with a sponge layer. Velocity profiles in comparison with the log law.

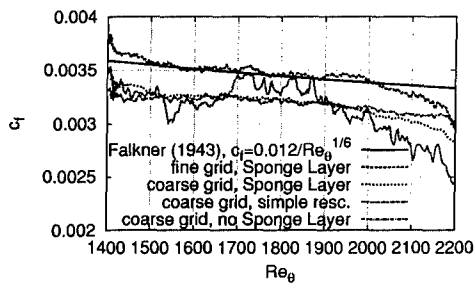

Figure 2. LES of a turbulent boundary layer for Re_{θ_o}=1400 and M=0.4. Skin-friction coefficient in comparison with Falkner's formula.

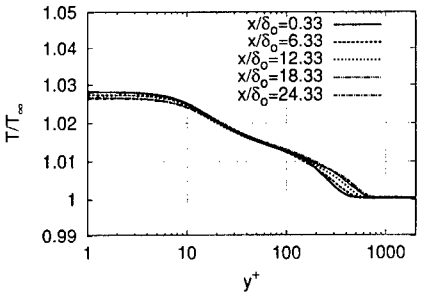

Figure 3. LES of a turbulent boundary layer for Re_{θ_o}=1400 and M=0.4. Temperature profiles at different streamwise locations.

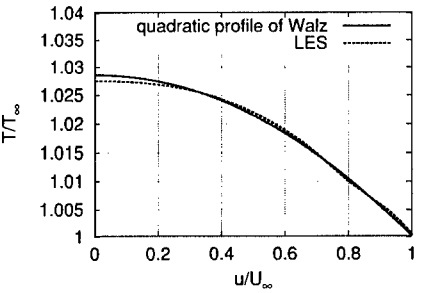

Figure 4. LES of a turbulent boundary layer for Re_{θ_o}=1400 and M=0.4 at Re_θ=1850. Temperature-velocity relationship compared with the profile of Walz [14].

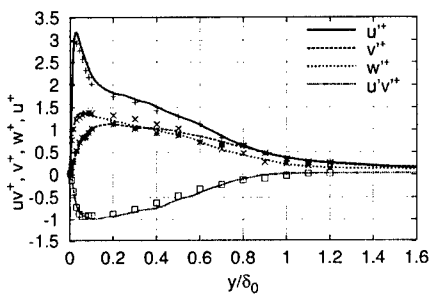

Figure 5. LES of a turbulent boundary layer for Re_{θ_o}=1400 and M=0.4 at Re_θ = 1850. Reynolds stress tensor components for the fine grid in comparison with the data of Lund et al.[8] (Symbols).

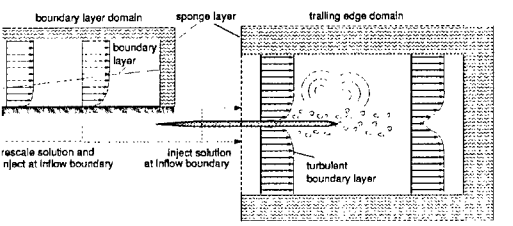

Figure 6. Sketch of the domain of integration for the boundary layer and trailing edge simulation.

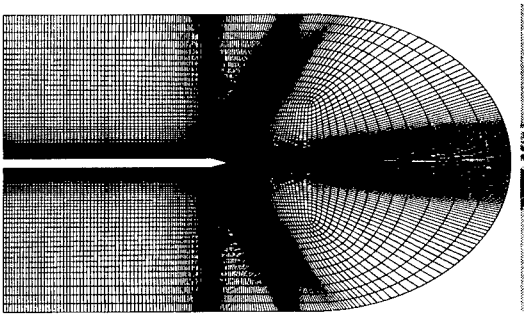

Figure 7. Grid for the LES of a turbulent flow over a sharp trailing edge. 2.25 Million grid points in 19 blocks. Every second grid point is shown.

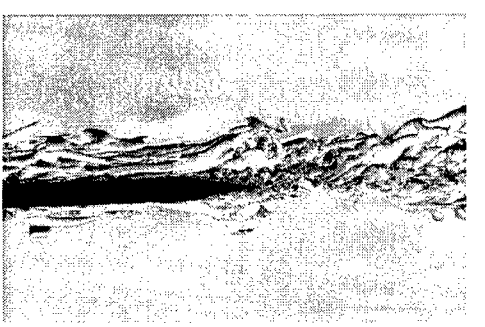

Figure 8. Visualization of the vortex structures in the boundary layer and in the near wake of the turbulent M = 0.15 flow around a sharp trailing edge.

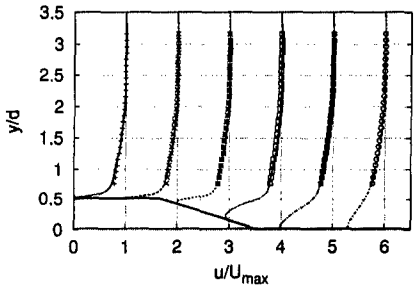

Figure 9. LES of a trailing-edge flow for $Re_\infty = 5.33 \times 10^5$ and M=0.15. Mean velocity profiles in the trailing-edge and the near-wake region compared with experimental data (Symbols).

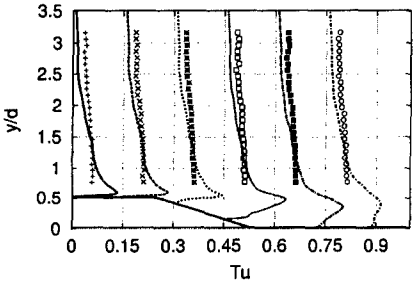

Figure 10. LES of a trailing-edge flow for $Re_\infty = 5.33 \times 10^5$ and M= 0.15. Turbulence kinetic energy profiles in the trailing-edge and the near-wake region compared with experimental data (Symbols).

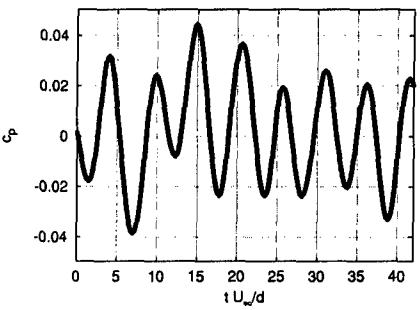

Figure 11. Time history of the surface pressure coefficient

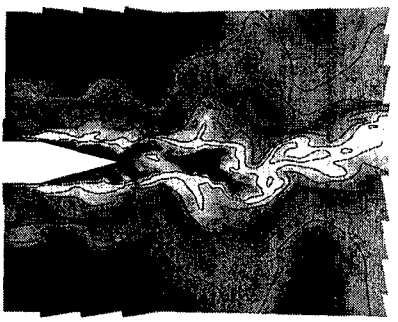

Figure 12. Instantaneous temperature distribution averaged in the spanwise direction.

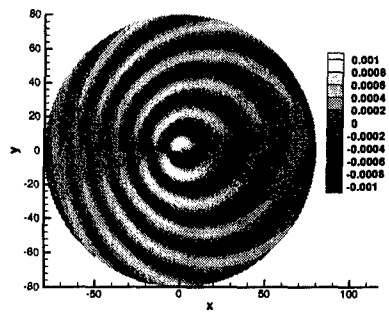

Figure 13. Instantaneous pressure distribution from the CAA solution, source term $-\rho_\infty \bar{D}\phi_v/Dt$.

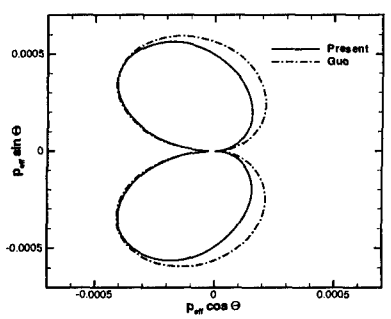

Figure 14. Directivity for the first harmonic frequency in comparison with Guo [5].